SISO Impedance-Based Stability Analysis for System-Level Small-Signal Stability Assessment of Large-Scale Power Electronics-Dominated Power Systems

Dongsheng Yang, *Senior Member, IEEE*, and Yin Sun, *Member, IEEE*

***Abstract*—To address the growing dynamic issues in the power electronics-based power system, this paper proposed an enhanced impedance-based stability analysis which can not only obtain the global view of system dynamics, but also provide a tailor-made stabilization solution by the direct use of the measured black-box models. With the proposed method, the dynamic interactions at selected multiple ports of the system are translated as multiple decoupled single-input single-output (SISO) minor loops in the frequency domain, of which the stability can be readily assessed by the SISO Nyquist stability criterion. Moreover, the oscillation mode shapes, i.e., the relative magnitude and phase of oscillated voltages and currents at the selected ports, are derived mathematically. Furthermore, the frequency-domain participation factor is defined to identify the most contributive components for the oscillations; Through impedance shaping solution of the corresponding oscillatory mode, it also provides the most effective system stability enhancement solution. EMTDC/PSCAD time-domain simulation results from an 800 MW offshore wind energy system with a realistic complexity confirm the effectiveness of the proposed method.**

***Index Terms*—System-level small-signal stability, impedance-based stability analysis, modal analysis, minor loop, Nyquist stability criterion, participation factor, impedance shaping.**

I. Introduction

TO MITIGATE climate change and secure sustainable energy supply, the global green-energy transitions are accelerating, and massive renewable energy resources are continuously integrated into electrical power grids [1]. As the key enabler for this transformation, the power electronic converters are widely used as efficient and flexible power processing units that interface with the power system and play an increasingly essential role in every sector of the electrical power grid, including the generation, transmission, distribution, and consumption [2].

Unlike centralized synchronous generators (SG) dominated power systems, hundreds of distributed converters may be present in the power-electronics-dominated system (such as the solar or wind farm). Moreover, the dynamics of power electronic converters are more dependent on the wide-time scale controllers rather than the law of physics [3], leading to an increasing number of non-characteristic harmonics and resonance incidents reported over a wide frequency range in recent years [4]–[7], which cause significant economic losses and poses great challenges to the safe operation of modern power grids. As a result, the scalable system-level small-signal stability analysis is urgently needed, which should not only identify the stability condition of the system (stable or not), but also be able to characterize the individual component's contribution to the instability and provide a tailor-made mitigation solution with the most effective design-oriented stabilization method.

The time-domain modal analysis based on the state-space model has been widely adopted to assess the multi-machine interactions as well as inter-area oscillations of the large-scale synchronous generator (SG)-dominated power systems for decades [8]. It gives a complete overview of the system dynamics in detail. Specifically, the eigenvalues and eigenvectors of the state matrix provide rich information about all the oscillatory modes, including their oscillation frequencies, damping ratios, and the oscillation mode shapes [8]–[11]. The participation factors reveal the dynamic contributions of state variables, and thus can be used for system damping control [8]. Despite the many advantages of modal analysis, there are very limited applications in the system-level stability analysis of power electronics-dominated power systems. This is mainly due to the significant obstacles in formulating the complete state-space model for the large-scale distributed power electronics dominated-power systems [3]. Firstly, with hundreds of power electronics converters in the system and each containing tens of states, it leads to a very high-order system state matrix and thus a high demand for computational power [12]. Secondly, the converter control algorithms are usually different from one vendor to another and are usually black-boxed and protected as intellectual property

Manuscript received April 15, 2021; revised August 27, 2021; accepted October 5, 2021. Date of publication October 11, 2021; date of current version December 16, 2021. Paper no. TSTE-00404-2021. *(Corresponding author: Dongsheng Yang.)*

Dongsheng Yang is with the Department of Electrical Engineering, Eindhoven University of Technology, 5612 AP Eindhoven, The Netherlands (e-mail: d.yang1@tue.nl).

Yin Sun is with the New Energies Research & Technology, Shell Global Solutions International BV, 2596 HP Den Haag, The Netherlands (e-mail: yin.sun@shell.com).

Color versions of one or more figures in this article are available at https://doi.org/10.1109/TSTE.2021.3119207.

Digital Object Identifier 10.1109/TSTE.2021.3119207

(IP) [13], which further prevents the accurate formulation of the state-space models. Therefore, the modal analysis cannot be readily applied for power electronics-dominated systems with multi-vendor converters.

As an alternative, the impedance-based analysis was originally developed to address local dynamic interactions between the converter and power grid at the point of connection (PoC) [14], [15]. Different from the state-space model, the impedance model of an electrical system is essentially the transfer function from its external voltage input to the current output (or vice versa for admittance), featuring good modularity and scalability [16]. Moreover, such impedance model can be measured by the external frequency scanning without disclosing the internal confidential details [17], [18]. Due to these advantages, many efforts have been made to extend the localized impedance-based analysis to the system-level stability assessment for power electronics-dominated power systems.

Different from the local stability analysis at a single PoC [19], multiple points will be analyzed simultaneously to obtain the global view of the system dynamics. As a result, the multi-input multi-output (MIMO) impedance matrix or admittance matrix needs to be used to reflect the MIMO dynamic relationships among the voltages and currents at selected points. Depending on the types of the impedance/admittance matrix that used, the existing system-level impedance-based analysis methods can be divided into closed-loop approaches [20]–[27] and open-loop approaches [28]–[32].

In [20], the closed-loop admittance matrix is formulated for the offshore wind farm by the closed-loop connection of all component admittances. The matrix zeros are then calculated to determine the system stability. Additionally, the bus participation factor is defined to rank the impacts of oscillations on different buses and identify the contributions from different power converters. Using the same stability criterion as [20], the frequency domain modal analysis (FMA) is proposed in [21] for the power systems with high penetration of renewables, and different participation factors are defined to identify the distribution of oscillations in the system and contributive components as well as to mitigate the oscillations. Since the direct calculation of the matrix zeros relies heavily on the explicit analytical expressions of transfer functions in the matrix, the analysis method in [20] and [21] requires disclosure of manufacture controller information at best, which is proven to be difficult. Although, in view of IP protection, it is practical to ask the vendor to provide the measured black-box impedance/ admittance model, to apply such model to the aforementioned analytical transfer function method requires curve fitting. Depending on the targeted order of the curve-fitted transfer function system, both errors and artificial poles/zeros can be introduced diminishing the value and accuracy of the end results.

To avoid the direct calculation of matrix zeros, the graphical FMA method can also be used for resonance analysis in traction systems [22], microgrids [23], wind power plants [24], and other converter-dominated systems [25]. By visually inspecting the resonance peak values in magnitude-frequency responses of the driving-point impedances at different buses or eigenvalues of the closed-loop impedance matrix, the resonance hazards can be identified. Moreover, the contribution of components to the resonance can be also quantified by the sensitivity analysis of these resonance peaks. However, the FMA studies in [22]–[25] only focus on the magnitude-frequency responses of the resonance modes, while the phase information was overlooked, thus they cannot distinguish negative damped resonances from positive ones. To address this issue, the quality factor rather than the magnitude of the resonant peak is used for FMA analysis [26], which can characterize both the positive and negative damping conditions of resonance mode, which is more suitable for the system that contains active components. Nevertheless, the calculation of the quality factor in [26] relies on a dedicated curve fitting method, namely "circle fit" [27], which assumes that all resonant modes can be represented by the second-order transfer function of a parallel RLC circuit individually. Thus, additional errors can be introduced during the curve fitting process, and deteriorate the accuracy of the FMA results.

Besides these closed-loop approaches, the generalized Nyquist stability criterion (GNC) can also be used to assess the closed-loop stability of the MIMO system from its open-loop impedance/admittance matrix or the so-called minor loop gain [28]–[29]. In order to apply GNC, the exact number of right-half-plane (RHP) poles in the minor loop gain has to be calculated [30]. The component connection method (CCM) is used to formulate the RHP-pole-free minor loop gain for multiple converter systems [31], which allows GNC stability analysis to be directly applied to the measured black-box models. However, since existing GNC-based analysis could not provide insight on the most effective impedance shaping method for system stabilization, it usually relies on an iterative design method to ensure system stability [31], [32].

This paper proposed an enhanced SISO impedance-based stability analysis (SISA) as an alternative open-loop system-level stability analysis method. As shown in Table I, compared with the state-space-based analysis, the proposed method has better modularity and scalability and can be directly applied on the measured black-box impedance/ admittance models without any model identification or curve fitting. Compared with other existing impedance-based analysis methods, for the first time, the proposed method can provide the mode shapes using black-box models, i.e., the relative magnitudes and phases of the oscillation at all ports under analysis, which not only gain a global view of the system dynamics but also provide a straightforward way to validate the accuracy of the stability analysis results. Moreover, it combines the advantages of other impedance-based analysis methods by providing the participation factor analysis, most-effective stabilization solution, and applicability on the pure black-box models at the same time, which makes it very promising for design-oriented system-level small-signal stability assessment for the large-scale power electronics-dominated power system.

II. System Representation

Fig. 1 shows the interactions of multiple power electronics applications in a generic power electronics-dominated power system. The components of interest are partitioned separately

TABLE I
COMPARISON OF DIFFERENT SYSTEM-LEVEL STABILITY ANALYSIS METHODS

Categories	State Space Based Analysis	Impedance Based Analysis				
Methods	Time-domain modal analysis	Frequency domain modal analysis (FMA)			Nyquist stability analysis	
Used models	State matrix	Closed-loop impedance/admittance matrix			Open-loop impedance /admittance matrix	
Stability criterion	Damping ratio of eigenvalues	Damping ratio of zeros	Magnitude of resonance peaks	Quality factor of resonance peaks	Generalized Nyquist stability criterion	SISO Nyquist stability criterion
Oscillation mode shapes	+	−	−	−	−	+
Participation factor analysis	+	+	+	+	−	+
Most effective stabilization solution	+	+	−	−	−	+
Modularity and scalability	−	+	+	+	+	+
Applicable on pure black-box models	−	−	+	+/−	+	+
References	[8]-[11]	[20],[21]	[22]-[25]	[26],[27]	[28]-[32]	Proposed SISA method

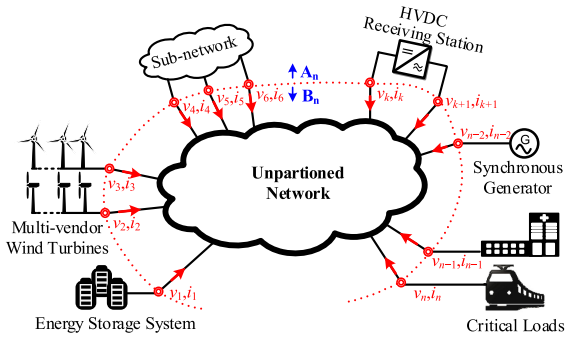

Fig. 1. Single-line diagram of a generic power electronics-dominated power system with multiple dynamic interactions.

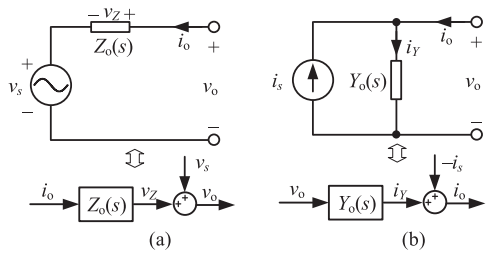

Fig. 2. Equivalent circuit and block diagram of the single port system based on (a) Thevenin theorem and (b) Norton Theorem.

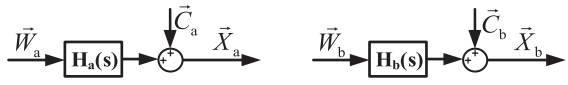

Fig. 3. Equivalent block diagram of (a) subsystem $\mathbf{A_n}$ and (b) subsystem $\mathbf{B_n}$.

from the network, and each component may contain one (e.g., energy storage system, a string of wind turbines, a critical load, etc) or multiple ports (e.g., a sub-network, an HVDC stations [33], etc).

To simplify the system representation, all of the portioned components can be modularized together as a single subsystem $\mathbf{A_n}$. Similarly, the rest of the unpartitioned network can also be modularized as a single subsystem $\mathbf{B_n}$. In this way, the dynamic interactions among multiple components and the unpartitioned network can be translated into the dynamic interaction between two subsystems $\mathbf{A_n}$ and $\mathbf{B_n}$ through the selected n ports.

To analyze the dynamic interactions between $\mathbf{A_n}$ and $\mathbf{B_n}$, the subsystem $\mathbf{A_n}$ and $\mathbf{B_n}$ are firstly disconnected from each other and are modeled separately in the frequency domain.

Take a single port subsystem as the example, if the terminal current i_o is chosen as the input variable, and the terminal voltage v_o is chosen as the output variable, then based on the Thevenin theorems, the impedance Z_o (s) in series with an independent voltage source v_s can be used to characterize the input current-output voltage relationship [14], as shown by the circuit and block diagram in Fig. 2(a). Based on the duality principle, the admittance Y_o (s) in parallel with an independent current source i_s can be used to characterize the input voltage-output current relationship based on the Norton theorem, as shown in Fig. 2(b).

As subsystem $\mathbf{A_n}$ contains n ports, there will be n input variables and n output variables. If all the input variables are the terminal currents that flow into n ports, then an impedance matrix with a voltage source vector have to be utilized to map the multi-input multi-output (MIMO) relationships of $\mathbf{A_n}$. However, for a more generic case, the input variables of $\mathbf{A_n}$ can be hybrid of voltages and currents, thus, the hybrid parameter matrix $\mathbf{H_a(s)}$[34], together with independent sources $\vec{C}_a$ are required to map the multi-input multi-output relationship at n ports, and its block diagram can be depicted by Fig. 3(a), where $\vec{W}_a$ and $\vec{X}_a$ are the input and output vectors, respectively. The diagonal elements of $\mathbf{H_a(s)}$ are the driving-point impedances/admittances at individual ports, while the non-diagonal elements of $\mathbf{H_a(s)}$ are mutual impedances/admittances between different ports. Each element of $\mathbf{H_a(s)}$ can be obtained using the frequency scanning method [17]–[18].

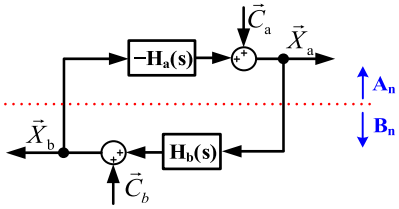

Fig. 4. Representation of power electronics-dominated power system in the frequency domain.

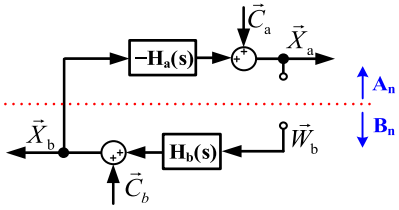

Fig. 5. Breaking the closed-loop system at $\vec{X}_{\rm a}$.

Similarly, the hybrid parameter matrix $\mathbf{H_b(s)}$ together with independent sources $\vec{C}_{\rm b}$ can be used to characterize the MIMO relationship of $\mathbf{B_n}$ at *n* ports, as shown in Fig. 3(b), where $\vec{W}_{\rm b}$ and $\vec{X}_{\rm b}$ are the input and output vectors, respectively. To represent the interactions of two subsystems, outputs of $\mathbf{A_n}$ should be used as inputs of $\mathbf{B_n}$, and vice versa.

As a result, the system in Fig. 1 can be simplified into Fig. 4 by connecting block diagrams of $\mathbf{A_n}$ and $\mathbf{B_n}$. The minus sign of $\mathbf{H_a(s)}$ in Fig. 4 is introduced by the non-associated reference directions of voltages and currents defined for $\mathbf{A_n}$, i.e., the outflowing currents rather than inflowing currents are defined as the positive for $\mathbf{A_n}$, as shown in Fig. 1.

To simplify the stability analysis, the RHP-pole-free partition rule is to partition all active components into one subsystem $\mathbf{A_n}$, so that $\mathbf{B_n}$ only contains passive components. As a result, the RHP-pole-free $\mathbf{H_a(s)}$ and $\mathbf{H_b(s)}$ can be formulated assuming all the active components are internally stable, and they are modeled as Thevenin equivalent when can be stably connected to the ideal current sources, while modeled as Norton equivalent when can be stably connected to the ideal voltage sources [31].

III. Stability Criterion of SISO Impedance-Based Stability Analysis (SISA)

For clarity, the matrices are denoted with capital boldface letters (e.g., $\mathbf{H_a}$) and their elements are denoted with lower-case italic letters (e.g., h_{a_ij}); the vectors are denoted with capital italic letters with are accented with right arrows (e.g., $\vec{X}_{\rm a}$), and their elements are denoted with either lower-case italic letters (e.g., x_{a_i}) or simply use an index to cite the vector (e.g., $\vec{L}_k(i)$). For simplicity, the Laplace variable $s = j\omega$ in signals and transfer functions are omitted in the following analysis.

To assess the closed-loop stability of $\vec{X}_{\rm a}$, the closed-loop in Fig. 4 can be first opened at $\vec{X}_{\rm a}$, as shown in Fig. 5. Thus, the open-loop response of $\vec{X}_{\rm a}$ resulting from the input $\vec{W}_{\rm b}$ and excitation sources $\vec{C}_{\rm a}$ and $\vec{C}_{\rm b}$ can be calculated based on the superposition theorem, expressed as

$$\vec{X}_{\rm a} = -\mathbf{H_a H_b}\cdot\vec{W}_{\rm b} + \vec{C}_{\rm a} - \mathbf{H_a}\vec{C}_{\rm b} \tag{1}$$

The closed-loop response of $\vec{X}_{\rm a}$ can be thereby obtained by letting $\vec{W}_{\rm b} = \vec{X}_{\rm a}$ in (1), i.e.,

$$\vec{X}_{\rm a} = -\underbrace{\mathbf{H_a H_b}}_{\mathbf{H}}\vec{X}_{\rm a} + \underbrace{\vec{C}_{\rm a} - \mathbf{H_a}\vec{C}_{\rm b}}_{\vec{C}} \tag{2}$$

where $\mathbf{H}$ is the open-loop transfer function matrix; $\vec{C}$ is the equivalent independent system inputs seen at $\vec{X}_{\rm a}$.

For a specific frequency ω, the elements of $\mathbf{H}$ are complex numbers. Therefore, by applying the eigenvalue decomposition [35], it yields

$$\mathbf{H} = \mathbf{R\Lambda L} \tag{3}$$

where Λ is a diagonal matrix whose diagonal elements are the eigenvalues of $\mathbf{H}$; $\mathbf{R}$ is a matrix whose column *k* is the unitized right eigenvector of $k^{\rm th}$ eigenvalue, denoted as $\vec{R}_k$; $\mathbf{L}$ is a matrix whose row *k* is the unitized left eigenvector of $k^{\rm th}$ eigenvalue, denoted as $\vec{L}_k$. They have the following properties.

$$\mathbf{HR} = \mathbf{R\Lambda} \tag{4}$$

$$\mathbf{LH} = \mathbf{\Lambda L} \tag{5}$$

$$\mathbf{L}^{-1} = \mathbf{R} \tag{6}$$

$$\vec{R}_k = \mathbf{R}\left(k,:\right), \vec{L}_k = \mathbf{L}\left(:,k\right) \tag{7}$$

$$\vec{L}_i \cdot \vec{R}_j = \begin{cases} 1 & i = j \\ 0 & i \neq j \end{cases} \tag{8}$$

Substituting (3) into (2), it yields

$$\vec{X}_{\rm a} = -\mathbf{R\Lambda L}\vec{X}_{\rm a} + \vec{C} \tag{9}$$

Left-multiplying $\mathbf{L}$ at both sides of Eq.(9), it gives

$$\mathbf{L}\vec{X}_{\rm a} = -\mathbf{\Lambda L}\vec{X}_{\rm a} + \mathbf{L}\vec{C} \tag{10}$$

By defining the equivalent vectors as

$$\vec{X}_{\rm eq} := \mathbf{L}\vec{X}_{\rm a} \tag{11}$$

$$\vec{C}_{\rm eq} := \mathbf{L}\vec{C} \tag{12}$$

Eq. (10) can be rewritten as

$$\vec{X}_{\rm eq} = -\mathbf{\Lambda}\vec{X}_{\rm eq} + \vec{C}_{\rm eq} \tag{13}$$

As Λ is a diagonal matrix, the arbitrary row in (13) can be represented in a scalar form as

$$x_{{\rm eq}\_k} = -\Lambda_k \cdot x_{{\rm eq}\_k} + c_{{\rm eq}\_k} \tag{14}$$

where $x_{{\rm eq}\_k}$ and $c_{{\rm eq}\_k}$ are the $k^{\rm th}$ elements of $\vec{X}_{\rm eq}$ and $\vec{C}_{\rm eq}$, respectively, while Λ_k is the $k^{\rm th}$ diagonal element of Λ.

Eq. (14) can be interpreted as the minor loop with unity gain in the forward path, and Λ_k in the negative feedback path, as shown in Fig. 6. As a result, the stability of the k^{th} minor loop can be readily assessed by the SISO Nyquist stability criterion.

When $\mathbf{H_a}$ and $\mathbf{H_b}$ are RHP-pole-free, the minor loop Λ_k will not contain RHP poles. Therefore, the minor loop Λ_k is stable

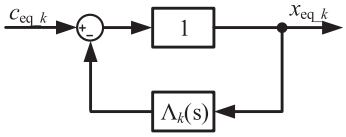

Fig. 6 The block diagram of k^{th} equivalent SISO minor loop.

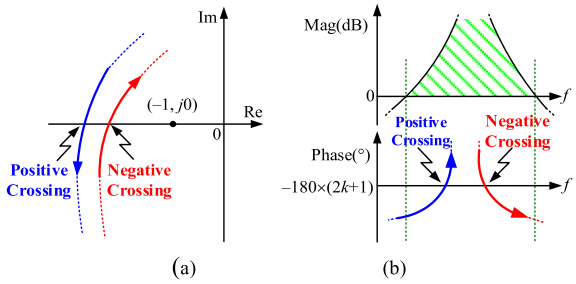

Fig. 7. Positive and negative crossings in (a) Nyquist plot and (b) Bode plot.

if and only if $N^+ - N^- = 0$, where N^+ and N^- are numbers of positive and negative crossings in the Nyquist/Bode plot of Λ_k at positive frequency range, respectively [36], as shown in Fig. 7 [37].

However, if RHP-pole-free cannot be guaranteed, the minor loop Λ_k may contain RHP poles. In this case, the number of RHP poles must be examined. By checking the magnitude slope change and the phase change of Λ_k, the number of RHP poles can be obtained [38], denoted as N_{RHP}. Thus, the minor loop Λ_k is stable if and only if $N^+ - N^- = N_{RHP}/2$ [37].

Similarly, the closed-loop response of $\vec{X}_\mathbf{b}$ can obtained

$$\vec{X}_\mathrm{b} = -\underbrace{\mathbf{H_b H_a}}_{\mathbf{H}'}\vec{X}_\mathrm{b} + \underbrace{\vec{C}_\mathrm{b} + \mathbf{H_b}\vec{C}_\mathrm{a}}_{\vec{C}'} \tag{15}$$

As seen, different open-loop transfer matrix $\mathbf{H}'$ will be obtained. Nonetheless, $\mathbf{H}'$ and $\mathbf{H}$ have the same eigenvalues [39] despite different eigenvectors. Due to the page limitation, SISA for $\vec{X}_\mathbf{b}$ will not be repeated in this paper.

IV. Oscillation Mode Shapes of SISA

According to (11), the output vector $\vec{X}_\mathrm{a}$ can be expressed in terms of equivalent output variables of the minor loops:

$$\begin{aligned}\vec{X}_\mathrm{a} &= \mathbf{L}^{-1}\vec{X}_\mathrm{eq} = \mathbf{R}\vec{X}_\mathrm{eq} = \sum_{k=1}^{n}\left[x_{\mathrm{eq\_}k}\cdot\vec{R}_k\right] \\ &= x_{\mathrm{eq\_1}}\cdot\vec{R}_1 + x_{\mathrm{eq\_2}}\cdot\vec{R}_2 + \ldots + x_{\mathrm{eq\_}n}\cdot\vec{R}_n\end{aligned} \tag{16}$$

This relationship bridges gaps between the dynamics of each minor loop and that of actual output variables. Take k^{th} minor loop as the example, the propagation of dynamics from its output $x_{\mathrm{eq\_}k}$ to the actual output variables $\vec{X}_\mathrm{a}$ can be described by Fig. 8, where $x_{\mathrm{a\_1}}, x_{\mathrm{a\_2}}, \ldots x_{\mathrm{a\_n}}$ are the elements of $\vec{X}_\mathrm{a}$, and $r_{\mathrm{k\_1}}, r_{\mathrm{k\_2}}, \ldots r_{\mathrm{k\_n}}$ are the elements of $\vec{R}_k$.

Although the minor loop may contain several critical oscillation modes at different frequencies, the distribution of each oscillation mode among the actual output variables is readily assessed by the right eigenvector at the corresponding frequency.

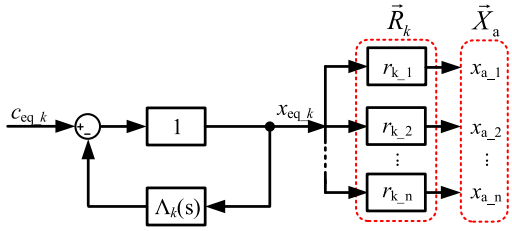

Fig. 8. Propagation of the dynamics from the output of k^{th} minor loop to actual output variables.

Assuming that there is a poorly damped or amplified oscillation that occurs in k^{th} minor loop at the frequency f_r, then this oscillation will propagate from the equivalent output variable $x_{\mathrm{eq\_}k}$ to the actual output variables $\vec{X}_\mathrm{a}$ in proportion to the k^{th} right eigenvector $\vec{R}_k$, .i.e.,

$$\vec{X}_\mathrm{a}(f_r) = \vec{R}_k(f_r)\cdot x_{\mathrm{eq\_}k}(f_r) \tag{17}$$

The right eigenvector $\vec{R}_k(f_r)$ provides a great insight into the relative magnitudes and phases of oscillations at each output variable, which could be used for stronger validation of stability analysis.

V. Participation Factor Analysis of SISA

To stabilize a critical minor loop, the sensitivity analysis will help to identify the most effective way of impedance shaping at the system level. More specifically, as for the sensitivity analysis, a small parameter perturbation can be applied to each element of $\mathbf{H}$ and then check the changes in the critical minor loop gains (i.e., eigenvalues) to determine which element has the most impact on the minor loop gains

According to (4) and (8),

$$\mathbf{H}\cdot\vec{R}_k = \Lambda_k\vec{R}_k \tag{18}$$

$$\vec{L}_k\cdot\vec{R}_k = 1 \tag{19}$$

Therefore, the k^{th} minor loop gain can be expressed as

$$\Lambda_k = \vec{L}_k\cdot\mathbf{H}\cdot\vec{R}_k \tag{20}$$

The sensitivity of k^{th} eigenvalue with respect of the element $h_{i,j}$ in $\mathbf{H}$ can be derived as

$$\begin{aligned}\frac{\partial\Lambda_k}{\partial h_{i,j}} &= \frac{\partial\left(\vec{L}_k\cdot\mathbf{H}\cdot\vec{R}_k\right)}{\partial h_{i,j}} \\ &= \frac{\partial\vec{L}_k}{\partial h_{i,j}}\cdot\mathbf{H}\cdot\vec{R}_k + \vec{L}_k\cdot\frac{\partial\mathbf{H}}{\partial h_{i,j}}\cdot\vec{R}_k + \vec{L}_k\cdot\mathbf{H}\cdot\frac{\partial\vec{R}_k}{\partial h_{i,j}} \\ &= \frac{\partial\vec{L}_k}{\partial h_{i,j}}\cdot\Lambda_k\cdot\vec{R}_k + \vec{L}_k\cdot\frac{\partial\mathbf{H}}{\partial h_{i,j}}\cdot\vec{R}_k + \Lambda_k\cdot\vec{L}_k\cdot\frac{\partial\vec{R}_k}{\partial h_{i,j}} \\ &= \vec{L}_k\cdot\frac{\partial\mathbf{H}}{\partial h_{i,j}}\cdot\vec{R}_k + \Lambda_k\frac{\partial\left(\vec{L}_k\cdot\vec{R}_k\right)}{\partial h_{i,j}}\end{aligned} \tag{21}$$

Since $\vec{L}_k\cdot\vec{R}_k = 1$ is a constant, $\frac{\partial(\vec{L}_k\cdot\vec{R}_k)}{\partial h_{i,j}}$ equals to zero. Moreover, since change $h_{i,j}$ will only affect the element at i^{th} row j^{th} column of $\mathbf{H}$, $\frac{\partial\mathbf{H}}{\partial h_{i,j}}$ is a matrix with all zero elements

except for the unity-gain element at i^{th} row j^{th} column, i.e.,

$$\frac{\partial \mathbf{H}}{\partial h_{i,j}} = \begin{bmatrix} \ddots & \vdots & \iddots \\ & 0\,0\,0 & \\ \cdots & 0\,1\,0 & \cdots \\ & 0\,0\,0 & \\ \iddots & \vdots & \ddots \end{bmatrix} \leftarrow i^{th}\ \text{row} \\ \uparrow j^{th}\ \text{column} \tag{22}$$

Therefore, (21) can be further simplified as

$$\frac{\partial \Lambda_k}{\partial h_{i,j}} = \vec{L}_k \cdot \frac{\partial \mathbf{H}}{\partial h_{i,j}} \cdot \vec{R}_k = \vec{L}_k(i) \cdot \vec{R}_k(j) \tag{23}$$

where $\vec{L}_k(i)$ is the i^{th} element of $\vec{L}_k$ and $\vec{R}_k(j)$ is the j^{th} element of $\vec{R}_k$.

The traditional participation factor in the state-space-based modal analysis is essentially the sensitivity of eigenvalues to the diagonal elements of the state matrix. However, this definition is not applicable in the frequency domain because the open-loop transfer function matrix $\mathbf{H}$ is the product of $\mathbf{H_a}$ and $\mathbf{H_b}$, and it is difficult to shape the diagonal elements $\mathbf{H}$ directly.

The most promising impedance shaping solution is to change the equivalent series impedance or shunt admittance at the selected ports, which are the diagonal elements of the $\mathbf{H_a}$ and $\mathbf{H_b}$. Therefore, a new participation factor is defined as the sensitivity of minor loop gain to the diagonal elements of $\mathbf{H_a}$ and $\mathbf{H_b}$.

By perturbing the i^{th} diagonal element $h_{\text{a\_}i,i}$ of matrix $\mathbf{H_a}$, it will change all the elements in row i of $\mathbf{H}$ due to the multiplication of $\mathbf{H_a}$ and $\mathbf{H_b}$, i.e.,

$$\begin{aligned} \vec{P}_{\text{a}k}(i) &:= \frac{\partial \Lambda_k}{\partial h_{\text{a\_}i,i}} \\ &= \sum_{c=1}^{n} \left(\frac{\partial h_{i,c}}{\partial h_{\text{a\_}i,i}} \cdot \frac{\partial \Lambda_k}{\partial h_{i,c}} \right) = \sum_{c=1}^{n} \left(h_{\text{b\_}i,c} \cdot \frac{\partial \Lambda_k}{\partial h_{i,c}} \right) \\ &= \sum_{c=1}^{n} \left(h_{\text{b\_}i,c} \cdot \vec{L}_k(i) \cdot \vec{R}_k(c) \right) \end{aligned} \tag{24}$$

where $h_{i,c}$ is the element of the matrix $\mathbf{H}$ at i^{th} row c^{th} column.

Similarly, by perturbing the i^{th} diagonal element $h_{\text{b\_}i,i}$ in of $\mathbf{H_b}$, it will change all the elements in column i of $\mathbf{H}$, i.e.,

$$\begin{aligned} \vec{P}_{\text{b}k}(i) &:= \frac{\partial \Lambda_k}{\partial h_{\text{b\_}i,i}} \\ &= \sum_{r=1}^{n} \left(\frac{\partial h_{r,i}}{\partial h_{\text{b\_}i,i}} \cdot \frac{\partial \Lambda_k}{\partial h_{r,i}} \right) = \sum_{r=1}^{n} \left(h_{\text{a\_}r,i} \cdot \frac{\partial \Lambda_k}{\partial h_{r,i}} \right) \\ &= \sum_{r=1}^{n} \left(h_{\text{a\_}r,i} \cdot \vec{L}_k(r) \cdot \vec{R}_k(i) \right) \end{aligned} \tag{25}$$

where $h_{r,i}$ is the element of the matrix $\mathbf{H}$ at r^{th} row i^{th} column.

As a result, the most promising shunt and series impedance shaping can be identified by ranking the participation factors defined in (24) and (25), i.e., the diagonal element with the greatest sensitivity to the critical minor loop gain can be selected for impedance shaping.

VI. Tailor-Made Impedance Shaping Method

To damp the oscillations, the critical minor loop must be adjusted to increase its stable margin. Assumed that the critical minor loop Λ_k has a unity-gain and a phase angle close to $-180°$

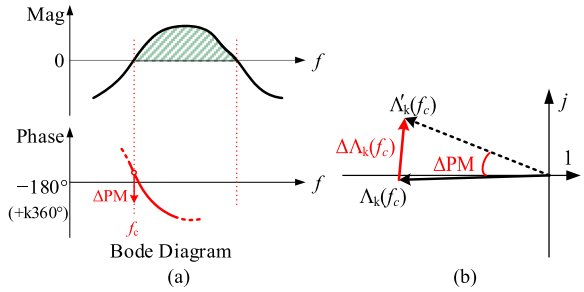

Fig. 9. Desirable adjustment for stabilizing the critical minor loop.

at the cross-over frequency f_c, which can be represented by a phasor, as shown in Fig. 9(a). One way to stabilize Λ_k is to increase the phase margin by ΔPM, which can be realized by rotating the phasor $\Lambda_k(f_c)$ with an angle of ΔPM, as shown by $\Lambda'_k(f_c)$ in Fig. 9(b). Therefore, the desirable adjustment for $\Lambda_k(f_c)$ can be calculated as

$$\begin{aligned} \Delta\Lambda_k(f_c) &= \Lambda'_k(f_c) - \Lambda_k(f_c) \\ &= \left(e^{-j\Delta\text{PM}} - 1\right) \cdot \Lambda_k(f_c) \end{aligned} \tag{26}$$

The proposed participation factor in (24) and (25) provides great insight on how to shape i^{th} diagonal impedance of $\mathbf{H_a}$ or $\mathbf{H_b}$. Assumed that the participation factor of i^{th} diagonal element in $\mathbf{H_a}$ has the largest magnitude, the desirable adjustment in (26) can be realized by shaping $h_{a\_i,i}$ at the cross-over frequency f_c as

$$\begin{aligned} &\Delta\Lambda_k(f_c) = \vec{P}_{\text{a}k}(i)(f_c) \cdot \Delta h_{a\_i,i}(f_c) \\ &\Rightarrow \Delta h_{\text{a\_}i,i}(f_c) = \frac{\Delta\Lambda_k(f_c)}{\vec{P}_{\text{a}k}(i)(f_c)} \triangleq g_i \cdot e^{j\delta_i} \end{aligned} \tag{27}$$

where $\vec{P}_{\text{a}k}(i)(f_c)$ is the i^{th} element in the participation factor $\vec{P}_{ak}$ at f_c; g_i and δ_i are the gain and the phase of $\Delta h_{\text{a\_}i,i}$.

A second-order bandpass filter with phase compensation can be used to implement shaping function $\Delta h_{\text{a\_}i,i}(s)$ in the frequency domain, which is expressed as

$$\Delta h_{\text{a\_}i,i}(s) = g_i \cdot \frac{2\omega_i \left(s\cos\delta_i - 2\pi f_c \sin\delta_i\right)}{s^2 + 2\omega_i s + (2\pi f_c)^2} \tag{28}$$

where ω_i is used as the quality factor.

It should be noted that the tailor-made impedance shaping function can be directly derived based on the measured black-box models without disclosing the internal control and circuit details of the power electronics converters, which can be used as the impedance shaping specifications for the multi-vendor power electronics converters.

Although the rigorous derivation of SISA method in Section III∼VI requires a lot of mathematical operations, the resulted implementation of SISA is rather simple, which can be depicted by the flowchart in Fig. 10. As seen, the major computation complexity lies in eigenvalue decomposition in (3). As the dimension of impedance matrix $\mathbf{H}$ used for eigenvalue decomposition is dependent on the number of selected ports rather than the number of system states, thus this computation complexity is lower than that of time-domain modal analysis.

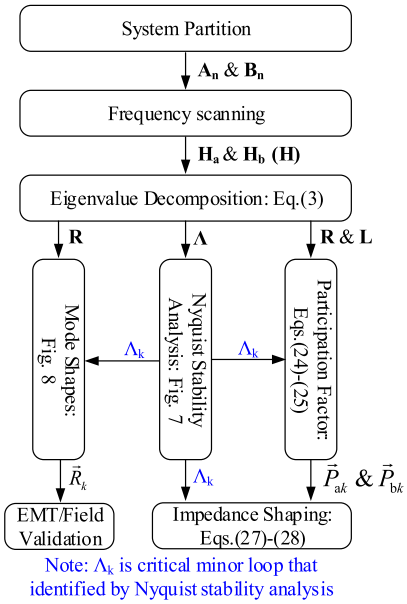

Fig. 10. Flowchart for implementation of the proposed SISA method.

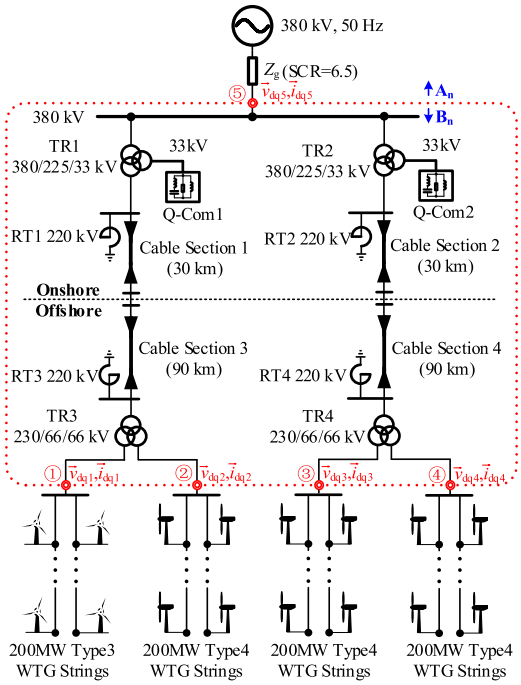

Fig. 11. The layout of an 800 MW wind energy system.

VII. Simulation Validation

A. System Description

An 800 MW wind energy system is built in the PSCAD/EMTDC v4.6.3 simulation software to validate the effectiveness of the proposed SISA, including the stability criterion, oscillation mode shapes and the impedance shaping based on the participation factor analysis. As shown in Fig. 11, four strings of 200 MW wind turbine generators (WTGs) are firstly connected to the 66 kV buses. After stepping up to 220 kV,

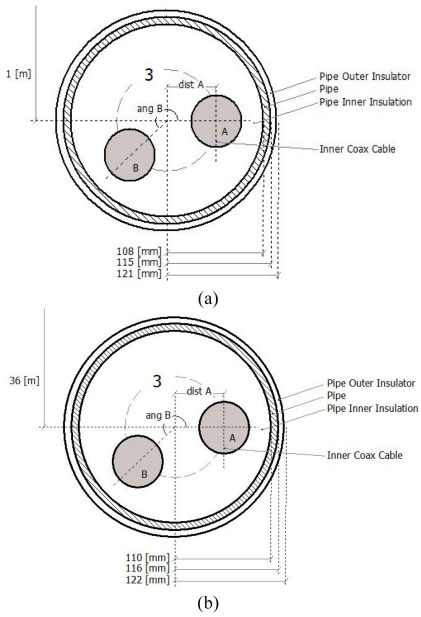

Fig. 12. Physical parameters and the dimensions of cable for (a) 30km onshore cable section 1 or 2. (b) 90 km offshore cable section 3 or 4.

the wind power is transported through a 90 km offshore cable section and a 30 km onshore cable section, and finally, feeds into 380 kV ac grid through onshore transformers.

Different 220 kV cables are selected for onshore and offshore cable sections. 1200 mm^2 copper is used as the core conductor of the onshore cable, while 1200 mm^2 aluminum is used as the core conductor of the offshore cable. Their physical parameters and the dimensions of the onshore and offshore cables used for frequency-dependent phase modeling are shown in Fig. 12. The electrical parameters of the cable sections are internally computed by the PSCAD/EMTDC v4.6.3 tool.

To increase the power transfer capacity, both onshore and offshore shunt reactors (RT1∼RT4) are installed to provide the necessary reactive power from two ends of the cables. The shunt reactor is modeled as an inductor L_{RT} in series connected with a resistor R_{RT}. In this paper, $L_{\mathrm{RT}} = 1.48$ H and $R_{\mathrm{RT}} = 0.648\ \Omega$ are selected.

The detailed electromagnetic transient (EMT) models of 2 MW type3 and type4 WTGs from PSCAD/EMTDC knowledge base [40] are utilized, where both the mechanical system and electrical system are modeled completely including 1) Wind turbine; 2) Pitch angle controller; 3). Grid-side converter and controls; 4) Machine-side converter and controls; 5) DC-link chopper protection; 6). Low pass filters; 7) Transformer; 8) Scaling component to increase the power level of WTG to model equivalent WTG strings. The default parameters of WTGs are adopted in this paper except for the base frequency (50 Hz) and the base voltage (66 kV).

B. Formulation of Hybrid-Parameter Matrices $\boldsymbol{H_a}$ and $\boldsymbol{H_b}$

The whole wind energy system is partitioned by the red dotted line is shown in Fig. 11, and five ports ①∼⑤ are selected for system-level stability analysis. Four strings of 200 MW WTGs

and the equivalent ac grid are treated as multiple-port system $\mathbf{A_n}$ and the rest transmission network is treated as multiple-port system $\mathbf{B_n}$.

The output variables for $\mathbf{A_n}$ and $\mathbf{B_n}$ are selected as

$$\vec{X}_{\mathrm{a}} = \begin{bmatrix} \vec{I}_{\mathrm{dq1}} \\ \vec{I}_{\mathrm{dq2}} \\ \vec{I}_{\mathrm{dq3}} \\ \vec{I}_{\mathrm{dq4}} \\ \vec{V}_{\mathrm{dq5}} \end{bmatrix} \vec{X}_{\mathrm{b}} = \begin{bmatrix} \vec{V}_{\mathrm{dq1}} \\ \vec{V}_{\mathrm{dq2}} \\ \vec{V}_{\mathrm{dq3}} \\ \vec{V}_{\mathrm{dq4}} \\ \vec{I}_{\mathrm{dq5}} \end{bmatrix} \tag{29}$$

Therefore, the hybrid-parameter transfer function matrix of $\mathbf{A_n}$ can be formulated accordingly

$$\mathbf{H_a} = \left[\begin{array}{cccc:c} \mathbf{Y_{WT3}} & & & & \\ & \mathbf{Y_{WT4}} & & & \\ & & \mathbf{Y_{WT4}} & & \\ & & & \mathbf{Y_{WT4}} & \\ \hdashline & & & & \mathbf{Z_g} \end{array}\right] \tag{30}$$

where $\mathbf{Y_{WT3}}$ and $\mathbf{Y_{WT4}}$ are the output admittance of type 3 and type 4 wind turbine strings seen from the 66 kV bus, respectively; $\mathbf{Z_g}$ is the equivalent impedance of the 380 kV ac grid; the rest of non-diagonal elements are zero. Since the wind turbines are stable when connected to an ideal 66 kV voltage source, and the equivalent impedance of the AC grid is passive, no RHP poles will appear in $\mathbf{H_a}$.

As for $\mathbf{B_n}$, it is relatively easier to measure its admittance matrix $\mathbf{Y_{matrix}}$, and then transform it into hybrid-parameter transfer function matrix $\mathbf{H_b}$. Considering the symmetry of the $\mathbf{B_n}$, the admittance matrix $\mathbf{Y_{matrix}}$ can be formulated as

$$\mathbf{Y_{matrix}} = \begin{bmatrix} \mathbf{Y}_1 & \mathbf{Y}_3 & \mathbf{Y}_4 & \mathbf{Y}_4 & \mathbf{Y}_5 \\ \mathbf{Y}_3 & \mathbf{Y}_1 & \mathbf{Y}_4 & \mathbf{Y}_4 & \mathbf{Y}_5 \\ \mathbf{Y}_4 & \mathbf{Y}_4 & \mathbf{Y}_1 & \mathbf{Y}_3 & \mathbf{Y}_5 \\ \mathbf{Y}_4 & \mathbf{Y}_4 & \mathbf{Y}_3 & \mathbf{Y}_1 & \mathbf{Y}_5 \\ \mathbf{Y}_6 & \mathbf{Y}_6 & \mathbf{Y}_6 & \mathbf{Y}_6 & \mathbf{Y}_2 \end{bmatrix} \triangleq \begin{bmatrix} \mathbf{Y_{11}} & \mathbf{Y_{12}} \\ \mathbf{Y_{21}} & \mathbf{Y_{22}} \end{bmatrix} \tag{31}$$

where diagonal elements $\mathbf{Y_1}$ and $\mathbf{Y_2}$ are self-admittances while $\mathbf{Y_3}\sim\mathbf{Y_6}$ are mutual-admittances.

In order to derive $\mathbf{H_b}$ from $\mathbf{Y_{matrix}}$, four sub-admittance-blocks of $\mathbf{Y_{matrix}}$ are defined, which can be expressed as

$$\mathbf{Y_{11}} = \begin{bmatrix} \mathbf{Y}_1 & \mathbf{Y}_3 & \mathbf{Y}_4 & \mathbf{Y}_4 \\ \mathbf{Y}_3 & \mathbf{Y}_1 & \mathbf{Y}_4 & \mathbf{Y}_4 \\ \mathbf{Y}_4 & \mathbf{Y}_4 & \mathbf{Y}_1 & \mathbf{Y}_3 \\ \mathbf{Y}_4 & \mathbf{Y}_4 & \mathbf{Y}_3 & \mathbf{Y}_1 \end{bmatrix}, \mathbf{Y_{12}} = \begin{bmatrix} \mathbf{Y}_5 \\ \mathbf{Y}_5 \\ \mathbf{Y}_5 \\ \mathbf{Y}_5 \end{bmatrix}$$

$$\mathbf{Y_{21}} = \begin{bmatrix} \mathbf{Y}_6 & \mathbf{Y}_6 & \mathbf{Y}_6 & \mathbf{Y}_6 \end{bmatrix}, \quad \mathbf{Y_{22}} = [\mathbf{Y}_2] \tag{32}$$

Therefore, the hybrid-parameter transfer function matrix $\mathbf{H_b}$ can be derived as [31]

$$\mathbf{H_b} = \begin{bmatrix} \mathbf{Y_{11}^{-1}} & -\mathbf{Y_{11}^{-1}Y_{12}} \\ \mathbf{Y_{21}Y_{11}^{-1}} & \mathbf{Y_{22}} - \mathbf{Y_{21}Y_{11}^{-1}Y_{12}} \end{bmatrix} \tag{33}$$

Since the transmission network only contains passive components, no RHP poles will appear in $\mathbf{H_b}$ either.

C. Black-Box Measurement of Elements in H_a and H_b

An advanced frequency-scanning toolbox is developed to automatize the measurement of the elements in $\mathbf{H_a}$ and $\mathbf{H_b}$, which can be seamlessly incorporated with the PSCAD/EMTDC software environment. The toolbox is modified from the impedance measurement automation toolbox that was developed for TSO, of which the accuracy has been verified by the vendor-specific black-box model of a real MMC-HVDC installation [41].

In this paper, frequency scanning is carried out from 1 Hz to 2 kHz with 160 equal-distance points in the log scale. The measured frequency responses of $\mathbf{Y_{WT3}}$, $\mathbf{Y_{WT4}}$, $\mathbf{Z_g}$, and $\mathbf{Y}_1\sim\mathbf{Y}_6$ in the global *dq*-frame at port ① are shown in Appendix as Figs. 23 and 24, respectively. It should be mentioned that $\mathbf{Y_{WT3}}$, $\mathbf{Y_{WT4}}$ are operating-point-dependent [42], therefore they should be measured at the operating point that is intended for system stability analysis.

D. Validations of SISA

Substituting the measured results in Fig. 23 into (30), $\mathbf{H_a}$ can be obtained; Substituting the measured results in Fig. 24 into (31) and then (33), $\mathbf{H_b}$ can be obtained. After that, the eigenvalues of open-loop transfer function matrix $\mathbf{H} = \mathbf{H_a}\mathbf{H_b}$ can be calculated as shown in Fig. 13, where Fig. 13(a) shows the critical minor loop Λ_9, while the rest of non-critical minor loops are shown in Fig. 13 (b), (c) and (d). While both Nyquist plots and Bode plots can be used to do stability analysis based on Nyquist stability criterion, the Bode plots can directly provide the essential frequency information that is needed for SISA, thus Bode plots are used to do SISO Nyquist stability analysis in this paper.

According to the most critical minor loop shown in Fig. 13(a), an oscillation at 27 Hz is expected in the wind energy system, as the phase margin is close to zero.

Fig. 14(a)∼(e) shows the voltage and current waveforms of the five ports from the EMT simulation, and growing oscillations can be observed. The beginning 4 seconds of oscillated waveforms are used for Fourier analysis. and the results are shown in Fig. 14(f). As seen, the oscillation frequency is around 27 Hz, which confirms the stability prediction of SISA.

The oscillation mode shapes, i.e., the relative magnitudes and phases of the voltage and current oscillations at the selected five ports are calculated according to (16), and are normalized at port ①, as shown in Fig. 15(a) and Fig. 16(a). As seen, the voltages and currents have completely different oscillation mode shapes. For comparison, the FFT analysis results at the oscillation frequency are also shown in Fig. 15(b) and Fig. 16(b), which show a good match with the SISA predictions in terms of both oscillation magnitudes and phase angles. The relative errors of calculated oscillation mode shapes compared with the simulated oscillation mode shapes in Fig. 15 and 16 are calculated as shown in Table II, where the maximum error is 4.71%, which validates the accuracy of the oscillation mode shapes obtained by the proposed SISA method.

To damp the oscillations, the critical minor loop must be adjusted to increase its stable margin. According to Fig. 13(a), the cross-over frequency Λ_9 is approximated to $f_{\mathrm{c}} = 27$ Hz.

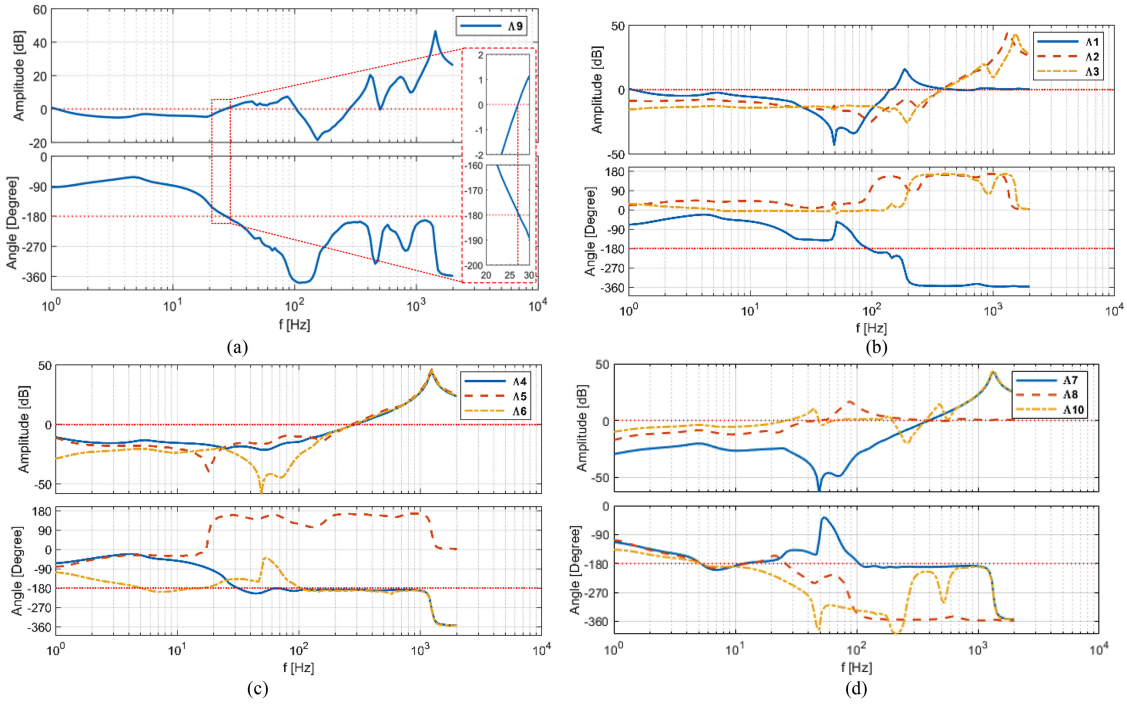

Fig. 13. Calculated frequency responses of minor loop gains (a) critical minor loop (b)–(d) non-critical minor loops.

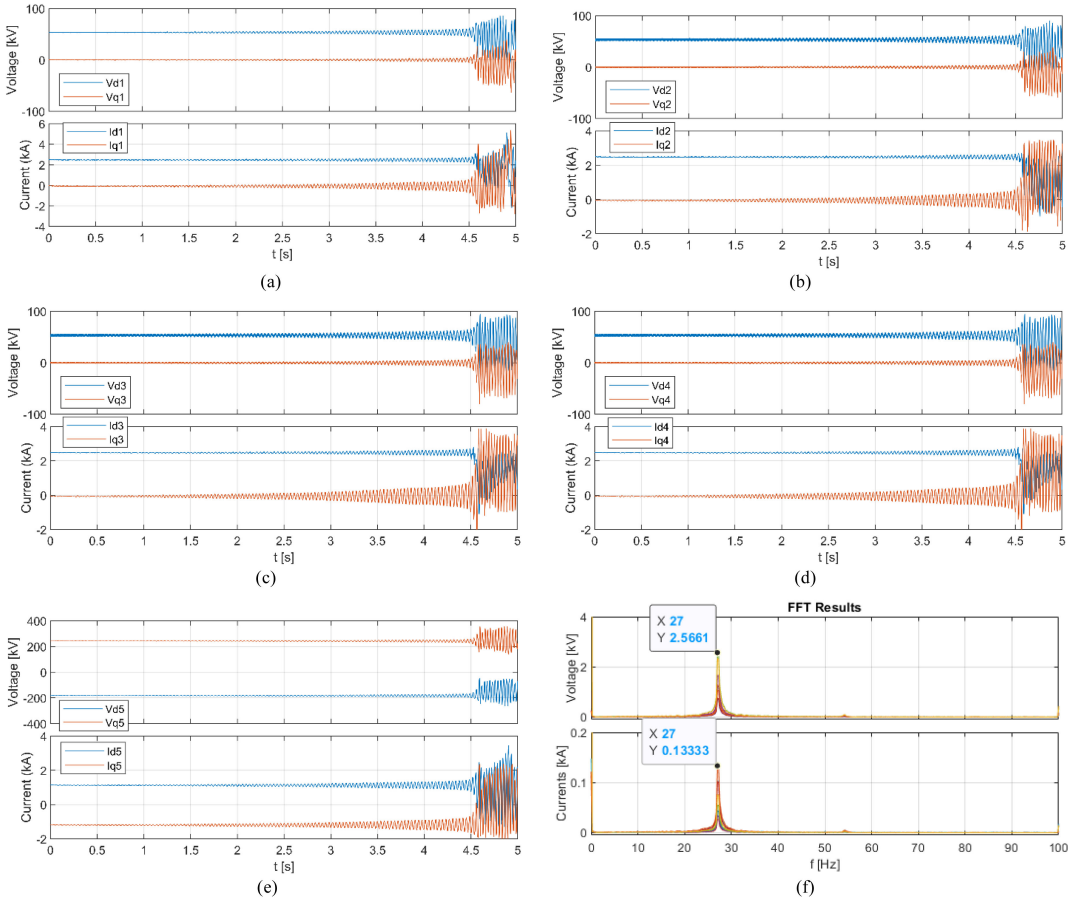

Fig. 14. EMT simulation waveforms of (a) port ① (b) port ② (c) port ③ (d) port ④ (e) port ⑤ and (f) their FFT analysis results.

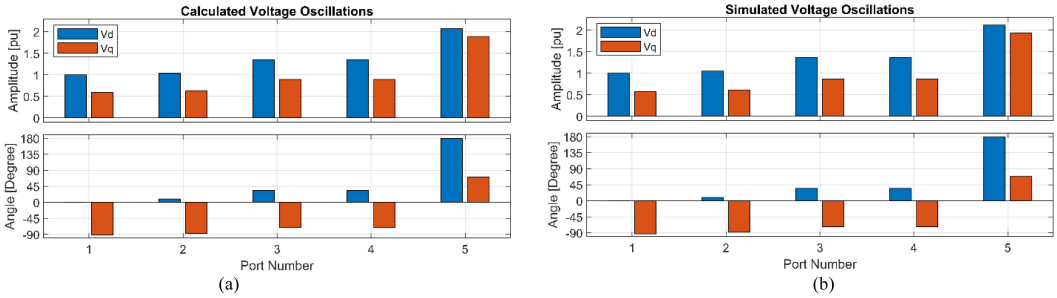

Fig. 15. Validation of the voltage oscillation mode shapes (a) Calculated results (b) Results from FFT analysis of EMT simulation waveforms.

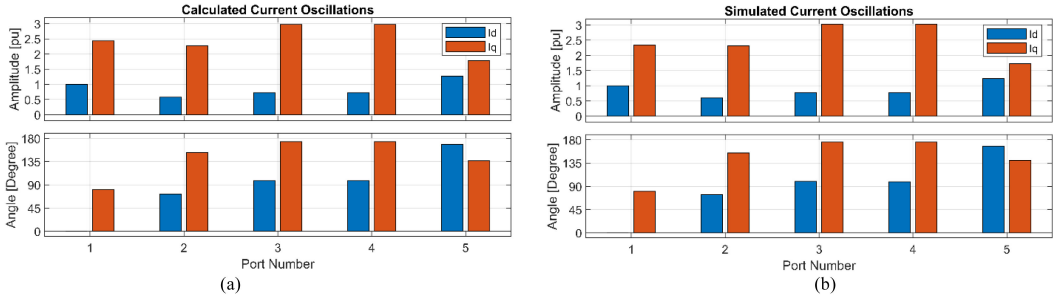

Fig. 16. Validation of the current oscillation mode shapes (a) Calculated results (b) Results from FFT analysis of EMT simulation waveforms.

TABLE II
RELATIVE ERROR OF MODE SHAPES

Port No.	Voltage magnitude	Voltage angle	Current magnitude	Current angle
1d	0	0	0	0
1q	3.83%	0.95%	3.31%	0.77%
2d	1.06%	2.76%	3.68%	1.83%
2q	3.01%	1.11%	1.93%	1.22%
3d	1.59%	1.41%	4.71%	0.83%
3q	2.73%	1.80%	1.58%	1.15%
4d	1.58%	1.41%	4.60%	0.72%
4q	2.73%	1.80%	1.55%	1.15%
5d	2.30%	0.34%	2.30%	0.04%
5q	2.07%	4.04%	3.08%	2.24%

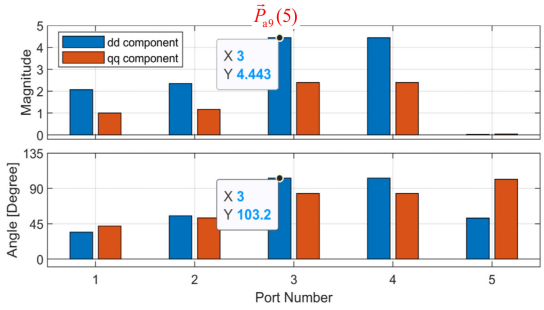

Fig. 17. Participation factor of $\mathbf{H_a}$ at f_c.

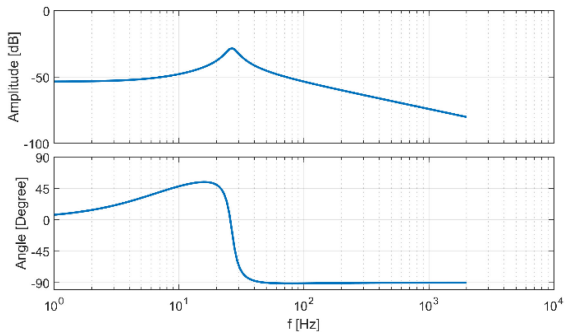

Fig. 18. The shunt shaping admittance at d-axis of port ③.

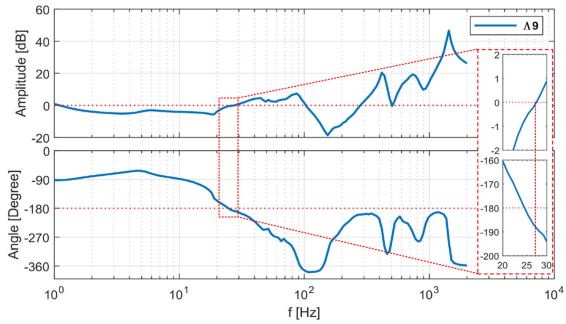

Fig. 19. The frequency response of shaped critical minor loop.

Accordingly, the participation factors $\vec{P}_{a9}$ at f_c can be calculated as shown in Fig. 17. It shows that dd components of ports ③ and ④ have the same and largest magnitude of participation factors, indicating both of them are dominated oscillation contributors, can be shaped to damp the oscillation most effectively. In this paper, the shaping of dd component at ports ③ (i.e., the fifth diagonal element of $\mathbf{H_a}$, $h_{a\_5,5}$) is taken as an example to validate the effectiveness of the participation factor.

Assuming an increase of phase margin $\Delta PM = 10°$ (i.e., $\pi/18$) at $f_c = 27$ Hz is selected as the shaping goal. According to (27),

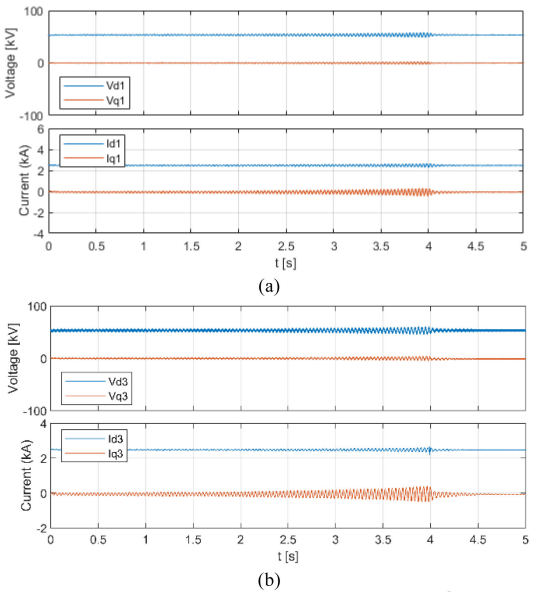

Fig. 20. Selected EMT Simulation waveforms of (a) port ① (b) port ③ with the impedance shaping enabled at 4s.

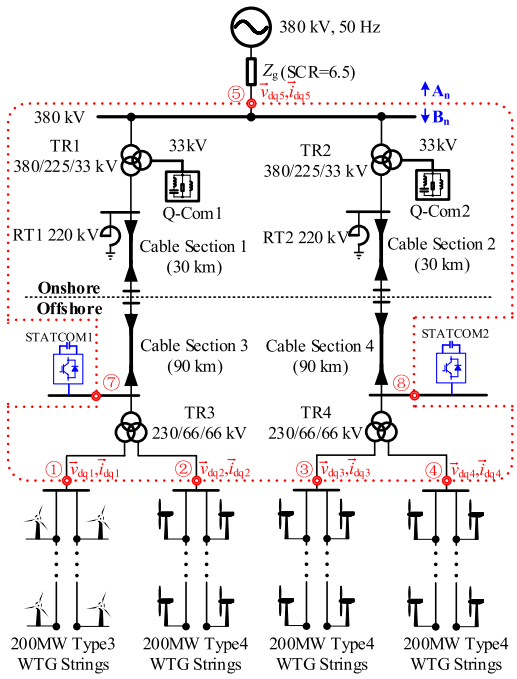

Fig. 21. RHP-pole-free portion rule for the scenario when additional active STATCOMs are installed offshore.

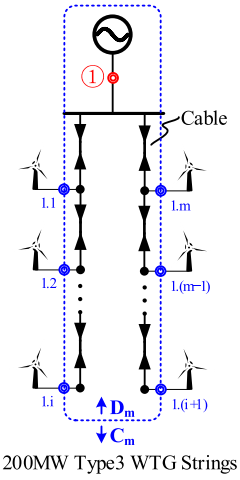

Fig. 22. Internal dynamic interaction analysis of WTG Strings at port ①.

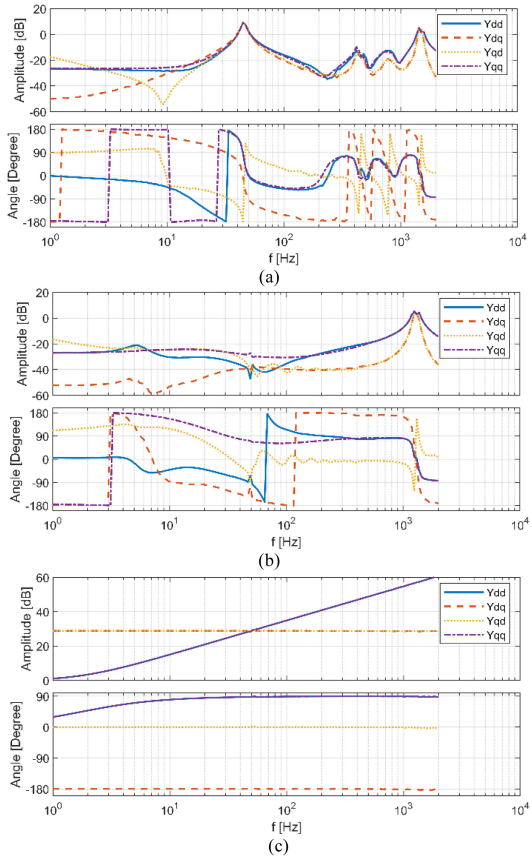

Fig. 23. Frequency scanning results of (a) Y_{WT3}, (b) Y_{WT4}, and (c) Z_g.

the required adjustment of $h_{a\_5,5}$ at f_c can be obtained as $g_5 = 0.0384$ (−28.13 dB) and $\delta_5 = -18.2°$. With $\omega_i = 0.1^*2\pi f_c$, the frequency response of shaping function in (28) can be depicted as Fig. 18. After adding $\Delta h_{a\_5,5}(s)$ into the *dd* component of 3rd diagonal element of (30), the frequency response of the shaped critical minor loop gain is shown in Fig. 19. Compared with Fig. 13(a), the phase margin of the critical minor loop at f_c = 27 Hz is increased by 9.5°, which matches well with the shaping goal. Due to the bandpass filter, the impedance shaping precisely targets at the frequency range around f_c = 27 Hz.

The shaping admittance is implemented in EMT simulation as follows: 1) sense the three-phase voltages at the port ③, and transform them into the *dq*-frame; 2) feed the *d*-axis voltage into the transfer function defined by (33); 3) the output of the transfer function is then transformed back into *abc*-frame and controls a shunt three-phase current source that connected at port ③. In reality, this shaping admittance can be either realized

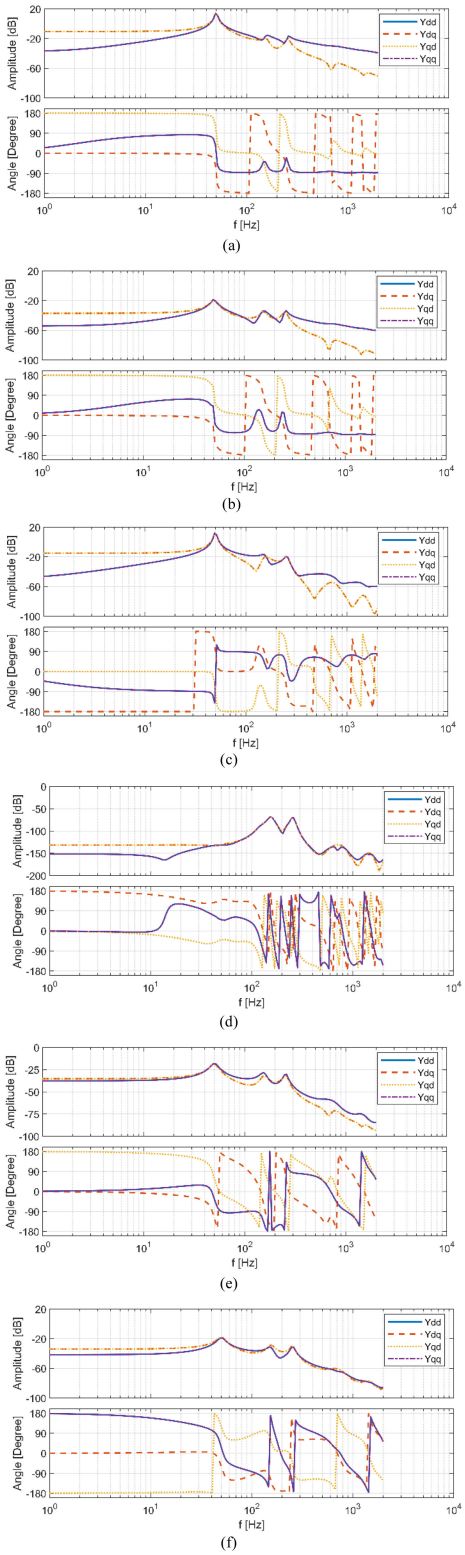

Fig. 24. Frequency scanning results of (a) $\mathbf{Y_1}$, (b) $\mathbf{Y_2}$, (c) $\mathbf{Y_3}$, (d) $\mathbf{Y_4}$, (e) $\mathbf{Y_5}$, and (f) $\mathbf{Y_6}$.

by the internal virtual impedance technique in the wind turbine converters [43] or the external active damper converter [44]. Due to the page limitation, the detailed realization of the shaping admittance at the converter level is out of the scope in this paper.

Selected simulation waveforms with impedance shaping are shown in Fig. 20. As seen, when the impedance shaping is enabled at 4 seconds, the growing oscillation is damped out rapidly, which verifies the effectiveness of the proposed participation factors of SISA in the impedance shaping for system-level stability enhancement.

E. Discussion on Generality of SISA

In this paper, subsystem $\mathbf{B_n}$ only contains passive network components. In real applications, the active components, such as STATCOMs, may be used for dynamic reactive power compensation instead of passive reactors RT3 and RT4. In this case, the RHP-pole-free condition can not be guaranteed for $\mathbf{H_b}$ when the same output variables in (29) are used. Therefore, minor loop gains may also contain RHP poles, and their number has to be examined for each minor loop gain individually, which complicates the SISO Nyquist stability analysis.

Alternatively, these STATCOMs can also be partitioned from the passive network just like the WTG strings, as shown in Fig. 21, which not only simplifies the Nyquist stability analysis of minor loop gains, and also helps to exam the contribution of the STACOMs to the oscillations.

Also, WTG strings are modularized as single units in previous system-level stability analysis, however, the internal dynamic interactions among the WTGs within a string can still be further analyzed by applying the proposed SISA again to the string level.

Take the Type 3 WTG string at port ① as the example, since the external interaction at port ① has been analyzed at the system level, an ideal voltage source can be used to replace the rest part of the system for the internal dynamic interaction analysis. More sub-ports 1.1∼1.m can be selected to partition the WTG strings into m-port sub-systems $\mathbf{C_m}$ and $\mathbf{D_m}$, as shown in Fig. 22. Thus, the internal dynamic interactions analysis can be readily assessed by following the same procedure as the previous system-level analysis. In this way, the dynamic interactions at different levels can be analyzed in a hierarchical way with reduced complexity as no need to address all the dynamic interactions at all levels at the same time.

Therefore, the proposed SISA demonstrates good generality for different system configurations and different levels of dynamics interactions.

VIII. Conclusion

This paper proposes a SISO impedance-based stability analysis that has great advantages over existing system-level stability methods by providing additional detailed information of oscillation mode shapes for a global view of oscillation distribution and the most effective impedance shaping solutions for system stability enhancement. More importantly, this method permits the direct utilization of the pure measured black-box impedances/admittance models. Therefore, it can readily be applied to the real-life large-scale power electronics-based power system with great complexity. The simulation results from an 800 MW offshore wind energy system with a realistic complexity confirm the effectiveness of the proposed analysis method.

APPENDIX

The measured frequency responses of $\mathbf{Y_{WT3}}$, $\mathbf{Y_{WT4}}$, $\mathbf{Z_g}$ are shown in Fig. 23, while the measured frequency responses of $\mathbf{Y}_1 \sim \mathbf{Y}_6$ are shown in Fig. 24.

REFERENCES

[1] P. Moriarty and D. Honnery, "Can renewable energy power the future?," *Energy Policy*, vol. 93, pp. 3–7, Jun. 2016.

[2] F. Blaabjerg, Z. Chen, and S. B. Kjaer, "Power electronics as efficient interface in dispersed power generation systems," *IEEE Trans. Power Electron.*, vol. 19, no. 5, pp. 1184–1194, Sep. 2004.

[3] X. Wang and F. Blaabjerg, "Harmonic stability in power electronic-based power systems: Concept, modeling, and analysis," *IEEE Trans. Smart Grid*, vol. 10, no. 3, pp. 2858–2870, May 2019.

[4] Wikipedia, "BARD offshore 1," Accessed: Aug. 9, 2020. [Online]. Available: https://en.wikipedia.org/wiki/BARD_Offshore_1

[5] North American Electric Reliability Corporation (NERC), "1,200 MW fault 627 induced solar photovoltaic resource interruption disturbance report," *Version 1.1*, Jun. 2017. [Online]. Available: https://www.nerc.com/pa/rrm/ea/1200_MW_Fault_Induced_Solar_Photovoltaic_Resource_/1200_MW_Fault_Induced_Solar_Photovoltaic_Resource_Interruption_Final.pdf

[6] L. Wang, X. Xie, Q. Jiang, H. Liu, Y. Li, and H. K. Liu, "Investigation of SSR in practical DFIG-based wind farms connected to a series compensated power system," *IEEE Trans. Power Syst.*, vol. 30, no. 5, pp. 2772–2779, Sep. 2015.

[7] C. Zou *et al.*, "Analysis of resonance between a VSC-HVDC converter and the AC grid," *IEEE Trans. Power Electron.*, vol. 33, no. 12, pp. 10157–10168, Dec. 2018.

[8] G. Rogers, *Power System Oscillations*. Boston, MA, USA: Springer, 2000.

[9] Y. Wang, X. Wang, Z. Chen, and F. Blaabjerg, "Small-signal stability analysis of inverter-fed power systems using component connection method," *IEEE Trans. Smart Grid*, vol. 9, no. 5, pp. 5301–5310, Sep. 2018.

[10] J. Beerten, S. D'Arco, and J. A. Suul, "Identification and small-signal analysis of interaction modes in VSC MTDC systems," *IEEE Trans. Power Del.*, vol. 31, no. 2, pp. 888–897, Apr. 2016.

[11] D. Yang and X. Wang, "Unified modular state-space modeling of grid-connected voltage-source converters," *IEEE Trans. Power Electron.*, vol. 35, no. 9, pp. 9700–9715, Feb. 2020.

[12] Y. Gu, N. Bottrell, and T. C. Green, "Reduced-order models for representing converters in power system studies," *IEEE Trans. Power Electron.*, vol. 33, no. 4, pp. 3644–3654, Apr. 2018.

[13] D. Yang Gong and X. Wang, "Impact analysis and mitigation of synchronization dynamics for DQ impedance measurement," *IEEE Trans. Power Electron.*, vol. 34, no. 9, pp. 8797–8807, Sep. 2019.

[14] J. Sun, "Impedance-based stability criterion for grid-connected inverters," *IEEE Trans. Power Electron.*, vol. 26, no. 11, pp. 3075–3078, Nov. 2011.

[15] L. Harnefors, L. Zhang, and M. Bongiorno, "Frequency-domain passivity based current controller design," *IET Power Electron,* vol. 1, no. 4, pp. 455–465, Dec. 2008.

[16] M. Amin and M. Molinas, "Small-signal stability assessment of power electronics based power systems: A discussion of impedance-and eigenvalue-based methods," *IEEE Trans. Ind. Appl.*, vol. 53, no. 5, pp. 5014–5030, Sep./Oct. 2017.

[17] B. Wen, D. Boroyevich, R. Burgos, P. Mattavelli, and Z. Shen, "Small-signal stability analysis of three-phase AC systems in the presence of constant power loads based on measured dq frame impedances," *IEEE Trans. Power Electron.*, vol. 30, no. 10, pp. 5952–5963, Oct. 2015.

[18] H. Gong, D. Yang, and X. Wang, "Impact analysis and mitigation of synchronization dynamics for DQ impedance measurement," *IEEE Trans. Power Electron.*, vol. 34, no. 9, pp. 8797–8807, Sep. 2019.

[19] N. Shabanikia, A. A. Nia, A. Tabesh, and S. A. Khajehoddin, "Weighted dynamic aggregation modeling of induction machine-based wind farms," *IEEE Trans. Sustain. Energy*, vol. 12, no. 3, pp. 1604–1614, Jul. 2021.

[20] E. Ebrahimzadeh, F. Blaabjerg, X. Wang, and C. L. Bak, "Bus participation factor analysis for harmonic instability in power electronics based power systems," *IEEE Trans. Power Electron.*, vol. 33, no. 12, pp. 10341–10351, Dec. 2018.

[21] Y. Zhan, X. Xie, H. Liu, H. Liu, and Y. Li, "Frequency-domain modal analysis of the oscillatory stability of power systems with high-penetration renewables," *IEEE Trans. Sustain. Energy*, vol. 10, no. 3, pp. 1534–1543, Jul. 2019.

[22] H. Hu, H. Tao, X. Wang, F. Blaabjerg, Z. He, and S. Gao, "Train–network interactions and stability evaluation in high-speed railways—Part II: Influential factors and verifications factors and verifications," *IEEE Trans. Power Electron.*, vol. 33, no. 6, pp. 4643–4659, Jun. 2018.

[23] Z. Liu, J. Rong, G. Zhao, and Y. Luo, "Harmonic assessment for wind parks based on sensitivity analysis," *IEEE Trans. Sustain. Energy*, vol. 8, no. 4, pp. 1373–1382, Oct. 2017.

[24] L. Hong, W. Shu, J. Wang, and R. Mian, "Harmonic resonance investigation of a multi-inverter grid-connected system using resonance modal analysis," *IEEE Trans. Power Del.,* vol. 34, no. 1, pp. 63–72, Feb. 2019.

[25] Y. Gu, Y. Li, Y. Zhu, and T. Green, "Impedance-based whole-system modeling for a composite grid via embedding of frame dynamics," *IEEE Trans. Power Syst.*, vol. 36, no. 1, pp. 336–345, Jan. 2021.

[26] S.-F. Chou, X. Wang, and F. Blaabjerg, "Frequency-domain modal analysis for power-electronic-based power systems," *IEEE Trans. Power Electron.*, vol. 36, no. 5, pp. 4910–4914, May 2021.

[27] J. He and Z.-F. Fu, *Modal Analysis*. London, U.K.: Butterworth Heinemann, 2001. [Online]. Available: http://www.sciencedirect.com/science/article/pii/B9780750650793500000

[28] X. Wang, L. Harnefors, and F. Blaabjerg, "Unified impedance model of grid-connected voltage-source converters," *IEEE Trans. Power Electron.*, vol. 33, no. 2, pp. 1775–1787, Feb. 2018.

[29] B. Wen, D. Dong, D. Boroyevich, R. Burgos, P. Mattavelli, and Z. Shen, "Impedance-based analysis of grid-synchronization stability for three-phase paralleled converters," *IEEE Trans. Power Electron.*, vol. 31, no. 1, pp. 26–38, Jan. 2016.

[30] M. Belkhayat, "Stability criterion for ac power systems with regulated loads," Ph.D. dissertation, Dept. Elect. Comput. Eng., Purdue Univ.,West Lafayette, IN, USA, 1997.

[31] W. Cao, Y. Ma, L. Yang, F. Wang, and L. M. Tolbert, "D–Q impedance based stability analysis and parameter design of three-phase inverter-based AC power systems," *IEEE Trans. Ind. Electron.*, vol. 64, no. 7, pp. 6017–6028, Jul. 2017.

[32] W. Cao, Y. Ma, and F. Wang, "Sequence-impedance-based harmonic stability analysis and controller parameter design of three-phase inverter-based multibus AC power systems," *IEEE Trans. Power Electron.*, vol. 32, no. 10, pp. 7674–7693, Oct. 2017.

[33] J. Beerten, S. D'Arco, and J. A. Suul, "Identification and small-signal analysis of interaction modes in VSC MTDC systems," *IEEE Trans. Power Del.*, vol. 31, no. 2, pp. 888–897, Apr. 2016.

[34] S. Chung and P. Roe, "Formulation and properties of hybrid matrices for (m +n)-port R networks," *IEEE Trans. Circuit Theory*, vol. 17, no. 2, pp. 243–245, May 1970.

[35] S. Skogestad and I. Postlethwaite, *Multivariable Feedback Control: Analysis and Design*. New York, NY, USA: Wiley, 2000.

[36] G. C. Goodwin, S. F. Graebe, and M. E. Salgado, *Control System Design.* Upper Saddle River, NJ, USA: Prentice-Hall, 2000.

[37] X. Ruan, X. Wang, D. Pan, D. Yang, W. Li, and C. Bao, *Control Techniques for LCL-Type Grid-Connected Inverters*. Singapore: Springer, 2018, pp. 176–177.

[38] Y. Liao and X. Wang, "Impedance-based stability analysis for interconnected converter systems with open-loop RHP poles," *IEEE Trans. Power Electron.*, vol. 35, no. 4, pp. 4388–4397, Apr. 2020.

[39] R. Bhatia, "Eigenvalues of AB and bA," *Resonance*, vol. 7, no. 1, pp. 88–93, Jan. 2002.

[40] PSCAD, "PSCAD Engineering Applications-Wind Power," Accessed: Sep. 8, 2020. [Online]. Available: https://www.pscad.com/knowledge-base/topic-47/v-

[41] D. Yang, X. Wang, M. Ndreko, W. Winter, R. Juhlin, and A. Krontiris, "Automation of impedance measurement for harmonic stability assessment of MMC-HVDC systems," in *Proc. Wind Integration Workshop*, Dublin, Ireland, 2019, pp. 1–6.

[42] M. Zhang, X. Wang, D. Yang, and M. G. Christensen, "Artificial neural network based identification of multi-operating-point impedance model," *IEEE Trans. Power Electron.*, vol. 36, no. 2, pp. 1231–1235, Feb. 2021.

[43] J. He and Y. W. Li, "Analysis, design, and implementation of virtual impedance for power electronics interfaced distributed generation," *IEEE Trans. Ind. Appl.*, vol. 47, no. 6, pp. 2525–2538, Nov. 2011.

[44] X. Wang, F. Blaabjerg, M. Liserre, Z. Chen, J. He, and Y. Li, "An active damper for stabilizing power-electronics-based AC systems," *IEEE Trans. Power Electron.*, vol. 29, no. 7, pp. 3318–3329, Jul. 2014.

Dongsheng Yang (Senior Member, IEEE) received the B.S., M.S., and Ph.D. degrees in electrical engineering from the Nanjing University of Aeronautics and Astronautics, Nanjing, China, in 2008, 2011, and 2016, respectively. In 2016, he joined Aalborg University, Aalborg, Denmark, as a Postdoc Researcher, where he became an Assistant Professor with the Department of Energy Technology in 2018. Since 2019, he has been with the Electrical Energy Systems Group, Eindhoven University of Technology, Eindhoven, The Netherlands, as an Assistant Professor. His main research interests include modeling, analysis, and control of large-scale power electronics-based power system, and advanced power conversion technologies for renewable energy generation, various industrial electrifications and renewable power to hydrogen. Dr. Yang was Technical Programme Vice Chair of IEEE COMPEL 2020 and Topic Chair of ECCE 2019. He was the recipient of the best paper awards at the IEEE IPEMC 2016, IEEE RPG 2017 and IEEE PEAC 2018.

Yin Sun (Member, IEEE) received the B.Sc. degree in electrical engineering from the Harbin Institute of Technology, Harbin, China, the M.Sc. degree in sustainable energy technology from Twente University, Enschede, The Netherlands, and the Ph.D. degree in stability and control of the power electronics dominant grid from the Eindhoven University of Technology, Eindhoven, The Netherlands, in 2008, 2010, and 2018, respectively. He is currently an Offshore Wind Electrical Innovation Lead of Shell, Subject Matter Expert (SME) of HVDC and power converters with Instrument Control and Electrical (ICE) Discipline, Shell Projects & Technology. Prior to joining Shell, he was with KEMA (predecessor of DNV GL Energy) from 2010 to 2019, as a Power System Consultant in the field of the power grid design/analysis, renewable grid compliance certification, detailed engineering for primary/secondary power equipment, and power project site-commissioning support. He was the Lead Power System Study Engineer for the Lake Turkana Wind Power Project delivering 300 MW clean energy to the Kenya power grid. He was also the Power System Package Manager of EMAL Phase 2 Project (total asset realization of 3.8 billion $) in Abu Dhabi responsible for the conceptual design of the power management system (PMS), power system dynamic/transient study, harmonic resonance analysis, plant-wide protection coordination and auditing, and detailed engineering of primary/secondary power component. From 2014 to 2019, he was a Senior Researcher with DNV GL Group Technology Research, Arnhem, The Netherlands, where he focused on the power electronics testing in the Flexible Power Grid Lab (part of KEMA Laboratories) and the application of hardware in the loop for the power electronics testing, such as, MMC-HVDC, MMC-STATCOM, WTG, Solar, and Storage. He was the Work Package Manager of EU Horizon 2020 Research Project PROMOTioN focusing on the grid-code compliance testing and model validation of the grid-connected power electronics interface using the Controller-Hardware-in-the-loop and Power-Hardware-in-the-loop techniques. Dr. Sun is also an International Technical Expert in the CIGRE C4. B4. JWG38 (Network Modeling for Harmonic Calculation), CIGRE C4.49 (Multi Frequency Stability of Converter-based Modern Power System), and IEC TC8-SC8A (large scale renewable grid integration).